Accepted Manuscript

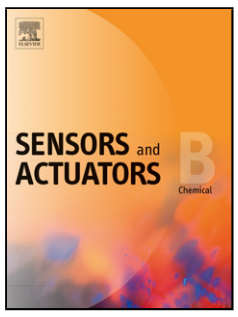

Title: Analysis of the kinetics of surface reactions on a zinc oxide nanosheet-based carbon monoxide sensor using an Eley-Rideal model

Author: Daniel R. Jones Thierry G.G. Maffeïs

PII: S0925-4005(15)00524-9
DOI: http://dx.doi.org/doi:10.1016/j.snb.2015.04.072
Reference: SNB 18377

To appear in: *Sensors and Actuators B*

Received date: 8-10-2014
Revised date: 20-3-2015
Accepted date: 19-4-2015

Please cite this article as: D.R. Jones, T.G.G. Maffeïs, Analysis of the kinetics of surface reactions on a zinc oxide nanosheet-based carbon monoxide sensor using an Eley-Rideal model, *Sensors and Actuators B: Chemical* (2015), http://dx.doi.org/10.1016/j.snb.2015.04.072

Analysis of the kinetics of surface reactions on a zinc oxide nanosheet-based carbon monoxide sensor using an Eley-Rideal model

Daniel R. Jones[1], Thierry G.G. Maffeïs[1]

1 *Multidisciplinary Nanotechnology Centre, Swansea University, Singleton Park, Swansea, SA2 8PP.*

Abstract

Herein, we experimentally test a mathematical model of the reactions on the surface of a zinc oxide nanosheet-based carbon monoxide sensor. The carbon monoxide is assumed to react with surface oxygen via an Eley-Rideal mechanism, considering only the direct reaction between the two species. We demonstrate that the measured resistance responses of the system are well described by the model, facilitating further analysis of the physical rate constants in the system. By initially considering the system in the absence of any reducing gas, it is shown that various reaction parameters may be precisely estimated. For instance, fitting the model to response curves obtained at different temperatures shows the activation energy of the reaction between oxygen ions and carbon monoxide to be 54 ± 9 kJ mol^{-1}, whereas the recovery curves yield an estimate of 42 ± 7 kJ mol^{-1}. Similarly, the energy barrier for the formation of oxygen ions is found to equal 72 ± 9 kJ mol^{-1} from the sensor response and 63 ± 10 kJ mol^{-1} from the recovery. These estimates are in agreement with values quoted elsewhere in the literature, corroborating the validity of the model. In the absence of surface ions, the energy difference between the Fermi level and the conduction band minimum at the surface is estimated as 590 ± 90 meV.

***Keywords**:* Eley-Rideal; CO sensor; Activation energy; Reaction mechanism; Fermi level.

Introduction

Metal oxide sensors have been the subject of intense research for many years because of their potential to produce small, inexpensive sensors capable of not only detecting a range of gases at levels of only a few parts per million, but also distinguishing between these gases in a selective manner. The unifying feature of many of these sensors is their use of a metal oxide such as SnO_2 [1, 2], TiO_2 [3, 4] or ZnO [5, 6], either as a thin polycrystalline film or in the form of nanostructures. Devices range from simple resistive sensors [7-12] to more complicated setups which utilise metallic gates [13, 14]. The basic sensing mechanism relies on changes in the conductivity of the metal oxide layer induced by surface chemical reactions between chemisorbed oxygen species and target gases. The sensors normally have their optimum sensitivity when operated at elevated temperatures (100^oC-400^oC).

Several groups have formulated theoretical models of metal oxide gas sensor response based on the underlying kinetics of the reactions on metal oxide surfaces at elevated temperatures. For systems containing surface catalysts such as noble metals, authors commonly employ a Langmuir-Hinshelwood reaction scheme between ionised surface oxygen and a reducing gas [15-21], which assumes that both species are adsorbed prior to their interaction. By considering the changing surface concentration of each species, it is possible to relate the rate of physical reactions to measured changes in the electrical resistance of the system. However, the differential equations corresponding to different surface species are typically coupled, making it difficult to fit the model to experimental data.

In the absence of surface catalysts, the complexity of the Langmuir-Hinshelwood model may be avoided by instead assuming an Eley-Rideal mechanism [19-26] for the reaction; in this regime, the reducing species reacts with oxygen ions directly, without first adsorbing to the surface. By neglecting adsorption of the reducing gas, there are fewer surface reactions to consider when constructing a physical description of the system. The simplicity of the Eley-Rideal process therefore facilitates modelling of the sensor response, enabling greater insight into the properties of the surface reactions.

In the present study, zinc oxide nanosheets are used to investigate the surface reactions of carbon monoxide. To study the formation of oxygen ions at the zinc oxide surface, the relationship between the sensor response and oxygen partial pressure is investigated prior to measuring the effects of the reducing gas. By considering only Eley-Rideal interactions between carbon monoxide and surface oxygen ions, rate constants are estimated for the adsorption, dissociation and ionisation of oxygen and the chemisorption of carbon monoxide molecules. Comparison of rate constant values obtained at different working temperatures makes it possible to estimate the activation energies of various surface reactions.

Model formulation

A simple model based on the kinetics of adsorption and desorption processes is derived as follows. As a starting point, it is assumed that each adsorbed oxygen molecule dissociates and removes electrons from the metal oxide surface, ionising to form two singly charged oxygen ions. In doing so, a positively charged depletion region is formed below the surface, increasing the electrical resistance of the metal oxide. In the absence of a reducing gas, the oxygen ions remain until they recombine to form diatomic oxygen, which lowers the electrical resistance as electrons are returned to the metal oxide.

When carbon monoxide is added to the system it may react with the surface oxygen ions, forming carbon dioxide and releasing electrons back to the metal oxide. It is proposed that the carbon monoxide chemisorbs to the surface oxygen prior to release of carbon dioxide, following an Eley-Rideal reaction mechanism.

The overall system is described by the reactions

$$\frac{1}{2}O_2 + site + e_S^- \xrightarrow{k_1} O^- \qquad (1)$$

$$O^- \xrightarrow{k_{-1}} \frac{1}{2}O_2 + site + e_S^- \qquad (2)$$

$$O^- + CO \xrightarrow{k_{r1}} CO_2^- \xrightarrow{kr2} CO_2 + site + e_S^- \qquad (3)$$

where the constants k_1 and k_{-1} are the rate constants for formation and desorption of surface O^- ions, respectively, while k_{r1} and k_{r2} correspond to the rate constants for the two steps of the irreversible reaction between the O^- ions and incident carbon monoxide via a reactive intermediate, CO_2^-. As shown in Eq. (1), O^- ions are created when an oxygen molecule dissociates at two unoccupied surface sites, referred to above as *site*, and becomes ionised by accepting two surface electrons, which are labelled as e_S^-. The electrons are returned to the metal oxide during the processes described by Eq. (2) and Eq. (3).

By combining the reactions, it is possible to describe how the concentration of surface ions changes with time. Adopting a similar approach to Nakata *et al*. [26], the concentration of O^- ions, $[O^-]$, varies according to

$$\frac{d[O^-]}{dt} = k_1\left(\frac{P_{O_2}}{P_{TOT}}\right)^{\frac{1}{2}}(n_{sites} - [O^-] - [CO_2^-]) - k_{-1}[O^-] - k_{r1}\left(\frac{P_{CO}}{P_{TOT}}\right)[O^-] \qquad (4)$$

where P_{O2} and P_{CO} are the partial pressures of O_2 and CO, respectively, and P_{TOT} is the total pressure in the system. Due to the reaction of O^- ions with CO from the gas phase, CO_2^- ions are present at a concentration labelled $[CO_2^-]$. The total concentration of surface sites (either unoccupied or containing a surface ion), is denoted by n_{sites} and assumed to remain constant. It is further assumed that the surface electrons, which appear as a reactant in Eq. (1), do not

take part in the rate-determining step of O^- ion formation, so the electron concentration does not appear in Eq. (4). This point is discussed further in the Supplementary Information.

As CO reacts with O^- ions, CO_2^- intermediates form at a rate given by

$$\frac{d[CO_2^-]}{dt} = k_{r1}\left(\frac{P_{CO}}{P_{TOT}}\right)[O^-] - k_{r2}[CO_2^-] \quad (5)$$

which follows directly from Eq. (3). Summing Eq. (4) and Eq. (5), one obtains the expression

$$\frac{d}{dt}([O^-] + [CO_2^-]) = k_1\left(\frac{P_{O_2}}{P_{TOT}}\right)^{\frac{s}{2}}(n_{sites} - [O^-] - [CO_2^-]) - k_{-1}[O^-] - k_{r2}[CO_2^-] \quad (6)$$

This equation does not depend on k_{r1}, as the conversion of O^- ions to CO_2^- intermediates does not alter the total concentration of surface ions. Dividing Eq. (6) by n_{sites},

$$\frac{d\theta_O}{dt} = k_1\left(\frac{P_{O_2}}{P_{TOT}}\right)^{\frac{s}{2}}(1-\theta_O) - k_{-1}\theta_O - (k_{r2} - k_{-1})\frac{[CO_2^-]}{n_{sites}} \quad (7)$$

where θ_O denotes the fraction of the total surface sites occupied by O^- or $[CO_2]^-$ ions, and is therefore defined by

$$\theta_O = \frac{[O^-] + [CO_2^-]}{n_{sites}} \quad (8)$$

It is useful to further consider the concentration of CO_2^- intermediates as a fraction of the total concentration of surface ions, which may be written as

$$\theta_{CO} = \frac{[CO_2^-]}{[O^-]+[CO_2^-]} \quad (9)$$

Substituting Eq. (9) into Eq. (7) yields

$$\frac{d\theta_O}{dt} = k_1(1-\theta_O)\left(\frac{P_{O_2}}{P_{TOT}}\right)^{1/2} - k_{-1}\theta_O - (k_{r2} - k_{-1})\theta_O\theta_{CO} \quad (10)$$

Similarly, division of Eq. (5) by the sum of $[O^-]$ and $[CO_2^-]$ produces the equation

$$\left(\frac{1}{[O^-]+[CO_2^-]}\right)\frac{d[CO_2^-]}{dt} = k_{r1}\left(\frac{P_{CO}}{P_{TOT}}\right)(1-\theta_{CO}) - k_{r2}\theta_{CO} \quad (11)$$

In the Supplementary Information it is shown that when θ_O changes sufficiently slowly, it is reasonable to replace Eq. (11) by the approximation

$$\frac{d\theta_{CO}}{dt} \approx k_{r1}\left(\frac{P_{CO}}{P_{TOT}}\right)(1-\theta_{CO}) - k_{r2}\theta_{CO} \quad (12)$$

More specifically, Eq. (12) is valid when $\ln(\theta_O)$ varies at a much lower rate than $\ln([CO_2^-])$. In this case, θ_{CO} does not explicitly depend on θ_O and the equation can therefore be solved analytically.

By imposing the condition that θ_{CO} is zero before CO is introduced into the system, Eq. (12) yields an expression for θ_{CO} which may be substituted into Eq. (10) to give

$$\frac{d\theta_O}{dt} + \theta_O\left(k_1\left(\frac{P_{O_2}}{P_{TOT}}\right)^{1/2} + k_{-1} + (k_{r2} - k_{-1})\frac{\varepsilon_{CO}}{\gamma_{CO}}(1 - \exp(-\gamma_{CO}t))\right) = k_1\left(\frac{P_{O_2}}{P_{TOT}}\right)^{1/2} \quad (13)$$

where

$$\gamma_{CO} = k_{r1}\left(\frac{P_{CO}}{P_{TOT}}\right) + k_{r2} \quad (14)$$

and

$$\varepsilon_{CO} = k_{r1}\left(\frac{P_{CO}}{P_{TOT}}\right) \quad (15)$$

It should be noted that time, t, is taken to be zero at the moment the CO is introduced to the system. Unfortunately Eq. (13) cannot be solved generally, but it is possible to obtain the steady-state solution, where $d\theta_O/dt$ is zero when t tends to infinity, which is given by

$$\theta_O(CO\ on) = \frac{K_O\left(\frac{P_{O2}}{P_{TOT}}\right)^{1/2}}{K_O\left(\frac{P_{O2}}{P_{TOT}}\right)^{1/2} + 1 + \left(\frac{k_{r2}}{k_{-1}} - 1\right)\frac{\varepsilon_{CO}}{\gamma_{CO}}} \quad (16)$$

where the ratio k_1/k_{-1} has been relabelled as a new parameter, K_O, the equilibrium constant for O^- formation.

The variation of θ_O and θ_{CO} during sensor recovery may be studied in a similar manner. Setting P_{CO} to zero in Eq. (12) and substituting the solution into Eq. (10) as before, θ_O is described by the equation

$$\frac{d\theta_O}{dt} + \theta_O\left(k_1\left(\frac{P_{O_2}}{P_{TOT}}\right)^{1/2} + k_{-1} + (k_{r2} - k_{-1})\frac{\varepsilon_{CO}}{\gamma_{CO}}\exp(-k_{r2}t)\right) = k_1\left(\frac{P_{O_2}}{P_{TOT}}\right)^{1/2} \quad (17)$$

Here, t is taken as zero at the moment that the CO is turned off. The steady-state solution of Eq. (17) is

$$\theta_O(CO\ off) = \frac{K_O\left(\frac{P_{O_2}}{P_{TOT}}\right)^{1/2}}{K_O\left(\frac{P_{O_2}}{P_{TOT}}\right)^{1/2} + 1} \quad (18)$$

It is now necessary to relate θ_O to the electrical resistance, R, of the sensor. This relationship has been derived previously by solving the Poisson Equation at the metal oxide surface [27, 28], yielding the formula

(19)

$$R(P_{O2}, T) = R_0(T)\exp(\alpha(T)\theta_O^2)$$

where α and R_0 are temperature-dependent constants. Eq. (19) is strictly only valid for sufficiently large particles, where the bulk material is unaffected by the electrical potential at the surface [28, 29]. The response of the sensor is defined by

$$Response = \frac{R(CO\ off) - R(CO\ on)}{R(CO\ off)} \quad (20)$$

where *R(CO on)* and *R(CO off)* correspond to the equilibrium resistance of the sensor when the CO is on and off, respectively. Used together, Eq. (19) and Eq. (20) provide a useful relationship between the fractional coverage of surface ions and the response.

The formulae derived thus far may now be used to predict how the response varies with changing P_{CO}/P_{TOT}. It will be demonstrated later that it is particularly informative to consider the reciprocal of Eq. (16), which, after substituting θ_O*(CO off)* into the expression using Eq. (18), can be written as

$$\frac{1}{\theta_O\,(CO\ on)} = \frac{1}{\theta_O\,(CO\ off)} + \frac{\left(\frac{k_{r2}}{k_{-1}} - 1\right)}{K_0\left(\frac{P_{O2}}{P_{TOT}}\right)^{1/2}} \frac{\varepsilon_{CO}}{\gamma_{CO}} \quad (21)$$

The advantage of Eq. (21) is that the P_{CO}/P_{TOT} dependence is confined to just one term. Moreover, if k_{r2} is much larger than the product of k_{r1} and P_{CO}/P_{TOT}, the final term becomes directly proportional to P_{CO}/P_{TOT} as γ_{CO} is approximately equal to k_{r2}. In this case, a plot of $1/\theta_O$(*CO on*) as a function of P_{CO}/P_{TOT} is expected to be linear.

Experimental

3.1. Sensor preparation

To support the sensing material, alumina gas-sensing substrates were purchased from the Electronics Design Centre at Case Western Reserve University, Cleveland, Ohio. These consisted of inter-digitated platinum electrodes mounted on alumina. Each electrode was spaced 300 µm from its neighbours, and alternate electrodes converged to form an electrical connection. A continuous platinum track was printed on the underside of each substrate to allow resistive heating of the sensor.

The ZnO nanosheets were produced by thermal decomposition of layered basic zinc acetate (LBZA) nanosheets, which were synthesised following a process described in our previous publication [30]. A 200 µL volume of rinsed LBZA nanosheets was drop-cast onto the inter-digitated platinum electrodes of a gas sensing substrate. After drying for several minutes at 60^{o}C, the substrate was annealed at 500^{o}C in a tube furnace under a 1 L min^{-1} flow of dry air for 30 minutes to thermally decompose the LBZA to ZnO. Following the heat treatment, the flow of dry air was continued until the furnace had cooled naturally back to room temperature.

3.2. Characterisation

The ZnO nanosheets were inspected prior to the gas sensing experiments using a Hitachi S4800 field emission scanning electron microscope at an accelerating voltage of 5 kV. In addition to the lengths and widths of the nanosheets, the sizes of the nanoparticles within each nanosheet were examined. Three different locations on the sample were scanned in order to evaluate the uniformity of the sensing material.

3.3. Oxygen and carbon monoxide sensing measurements

Sensing tests were conducted using a custom-built chamber. Nitrogen and oxygen gases were flowed separately through the chamber at rates controlled by mass-flow controllers, with the overall flow rate maintained at a constant value of 400 mL min^{-1}. The fraction of oxygen could be controlled accurately, and resistance measurements were taken at oxygen fractions (P_{O2}/P_{TOT}) between 0.05 and 0.2 in steps of 0.025. Hand-operated valves were used to switch between pure nitrogen gas and the test gas, which consisted of 1000 ppm carbon monoxide in nitrogen, and the rate of flow of the test gas was moderated by a mass flow controller to control the concentration of carbon monoxide present. Sensing tests were performed at carbon monoxide concentrations in the range 50–200 ppm, at intervals of 25 ppm.

The sample was heated by passing a current through the platinum track on the underside of the substrate. Prior to loading the substrate into the chamber, the resistance of the track was measured as a function of temperature using a K-type thermocouple. This calibration was used to deduce the temperature of the substrate during the sensing experiments. Both the current through the track and the potential difference across it were measured using two channels of a Keithley 2000 multimeter. The multimeter was also used to continuously measure the ZnO resistance during each sensing test.

Results and discussions

4.1. Sensor characterisation

SEM images of the ZnO nanosheets on the surface of the gas sensing substrate are shown in Fig. 1. Fig. 1(a) shows that the nanosheets are typically several microns across. In our previous publication [30], the nanosheet thickness was measured as 20–100 nm. The high resolution image in Fig. 1(b) shows that the sheets consist of multiple nanoparticles of varying shapes and sizes, with some apparent sintering observed. The average nanoparticle

diameter was determined to be 38nm, from more than 100 individual measurements, with a standard deviation of 18 nm. In order for Eq. (19) to be justified, the radius of each nanoparticle must be much greater than the width of the depletion region at its surface [28, 29]. However, without additional information regarding the concentration of donor states in the material, it is difficult to determine whether this condition is satisfied in the present system. It is therefore necessary to assess the applicability of Eq. (19) from the measured variation of the electrical resistance as a function of the oxygen partial pressure, as will be discussed later.

4.2. Estimation of α, R_0 and K_O

When formulating the model, it was mentioned that it is useful to express $1/\theta_O(CO\ on)$ as a function of P_{CO}/P_{TOT}, as in Eq. (21), an assertion which is justified by the observation that the two parameters are expected to exhibit a linear relationship when k_{r2} is sufficiently high. To realise why a direct proportionality between $1/\theta_O(CO\ on)$ and P_{CO}/P_{TOT} might be useful, it is instructive to first consider how both $\theta_O(CO\ on)$ and $\theta_O(CO\ off)$ may be determined from resistance measurements. According to Eq. (19), the resistance, R, is related to θ_O via two physical variables, namely R_0 and α. If the values of these parameters are known, it is therefore possible to deduce θ_O at any given time. Taking the natural logarithm of Eq. (19), $\ln(R)$ is expected to vary in direct proportion to θ_O^2. Moreover, the equation suggests that a plot of $\ln(R)$ as a function of θ_O^2 has gradient α and y-intercept $\ln(R_0)$, providing estimates for these two variables. Unfortunately, since θ_O cannot be measured directly, construction of the plot is not trivial.

In order to continue, Eq. (18) should be considered. This equation relates θ_O to P_{O2}/P_{TOT} in the absence of CO, through a third unknown parameter, K_O. Without additional information, it is clear that $\theta_O(CO\ off)$ cannot be calculated from measurements of P_{O2}/P_{TOT} as K_O is yet to be determined. However, after measuring R at multiple values of P_{O2}/P_{TOT} in the absence of CO, Eq. (18) and Eq. (19) may be used to construct multiple plots of $\ln(R)$ versus $\theta_O(CO\ off)^2$ for different "guess" values of K_O. For each K_O value, the gradient of the plot yields an estimate for α while the y-intercept is equal to $\ln(R_0)$. The requirement of a linear relationship potentially allows some of the K_O estimates to be discarded, as this behaviour does not necessarily exist for all of the guess values. Yet the value of K_O may not be sufficiently constrained by this consideration alone.

At this stage, it is helpful to investigate the relationship between R and P_{CO}/P_{TOT} at a particular value of P_{O2}/P_{TOT}. After measuring $R(CO\ on)$, Eq. (19) allows $\theta_O(CO\ on)$ to be calculated for each guess value of K_O from the corresponding estimates of α and $\ln(R_0)$. It is subsequently possible to plot $1/\theta_O(CO\ on)$ against P_{CO}/P_{TOT} for each K_O estimate. Provided that k_{r2} is much greater than $k_{r1}(P_{CO}/P_{TOT})$, $1/\theta_O(CO\ on)$ is expected to vary in direct proportion to P_{CO}/P_{TOT} with the y-intercept equal to $1/\theta_O(CO\ off)$. These requirements impose additional constraints on the value of K_O.

As an example, one may consider a value of K_O which results in a direct proportionality between ln(R) and P_{O2}/P_{TOT}. In addition, the corresponding plot of $1/\theta_O(CO\ on)$ versus P_{CO}/P_{TOT} at a particular P_{O2}/P_{TOT} value is linear over the measured range but the y-intercept does not equal the expected value of $1/\theta_O(CO\ off)$. This estimate of K_O is unsuitable, as it does not satisfy all of the requirements imposed by the theory. Although the relationship between $1/\theta_O(CO\ on)$ and P_{CO}/P_{TOT} plot is linear over the concentration range of the resistance measurements, the fact that the extrapolated y-intercept differs from the expected value of $1/\theta_O(CO\ off)$ indicates that this proportionality would not be observed at lower concentrations.

Fig. 2 illustrates an iterative procedure to determine K_O at a particular temperature. Starting with a guess value of K_O, a plot of ln(R) vs $\theta_O(CO\ off)^2$ is constructed and used to deduce the relationship between $1/\theta_O(CO\ on)$ and P_{CO}/P_{TOT} at constant P_{O2}/P_{TOT}. If the requirements of the two plots are not simultaneously satisfied by the K_O estimate, as described above, the guess value is modified and the procedure repeated. By iterating in this way, it is possible to obtain a well-constrained estimate of K_O, as well as the corresponding values of α and R_0.

4.3. Resistance measurements at different concentrations of oxygen

In order to obtain accurate estimates for α and R_0 at each working temperature, the resistance of the sensor was measured at different partial pressures of oxygen. The remainder of the gas environment consisted of pure nitrogen, with no CO present. According to Eq. (19), R is anticipated to exhibit an exponential relationship with θ_O^2 if the ZnO particles are sufficiently large. As shown by Fig. 3, this was observed experimentally at every temperature, with the gradients and y-intercepts providing estimates for α and ln(R_0), respectively. However, the form of each plot is dependent on K_O, and this is not well constrained by this experiment alone. As discussed, it is necessary to investigate the effects of CO to obtain more precise estimates of K_O. It should be noted that Fig. 3 has been constructed using the final K_O estimates obtained from the iterative approach outlined in Fig. 2.

4.4. Response measurements at different concentrations of carbon monoxide

In order to observe the relationship between $1/\theta_O(CO\ on)$ and P_{CO}/P_{TOT}, the response of the sensor was measured at different concentrations of CO with P_{O2}/P_{TOT} maintained at a value of 0.2 throughout. Plots of $1/\theta_O(CO\ on)$ versus P_{CO}/P_{TOT} are shown in Fig. 4; at each temperature, the K_O value used is the same as for the corresponding plot Fig. 3. There is a clear linearity in the results at every temperature, indicating that k_{r2} is much greater than $k_{r1}(P_{CO}/P_{TOT})$ and the second reaction step in Eq. (3) occurs much more rapidly than the first.

From Fig. 3 and Fig. 4, it is possible to infer the values of K_O, α and R_0. Together, these provide the means to fit the model to response and recovery curves and estimate further reaction parameters. However, the precision of the estimates is reliant on the effectiveness of

the iteration procedure outlined in Fig. 2. After using an initial value of K_O, $K_O(in)$, to plot $1/\theta_O(CO\ on)$ as a function of P_{CO}/P_{TOT}, the y-intercept provides a new K_O estimate, $K_O(out)$. If the two K_O values differ, $K_O(out)$ is used as the initial estimate in the next step of the iteration. As shown by Fig. 5, it is informative to consider the disparity between the two K_O values as a function of $K_O(in)$, as this determines the precision of the final K_O estimate yielded by the iteration process. To aid comparison between temperatures, the magnitude of the difference between $K_O(in)$ and $K_O(out)$ is expressed as a percentage of $K_O(in)$. At each temperature, it is apparent that the magnitude of the difference increases rapidly away from the point of agreement. The final value of K_O output by the iteration procedure is therefore well constrained, as even small deviations in the estimate lead to significant inconsistencies between $K_O(in)$ and $K_O(out)$.

It is apparent from Fig. 5 that there exists a temperature at which K_O is maximised. This is shown more explicitly in Fig. 6, which depicts K_O as a function of temperature. Also plotted is the response of the sensor, defined by Eq. (20), to 200 ppm CO. The peak response approximately coincides with the maximum K_O value, which suggests that the sensitivity of the sensor to CO is determined predominantly by the oxygen coverage. At the lower temperatures, there is a little energy available for the formation of O^- ions and hence K_O is low. Similarly, the reaction between CO molecules and O^- ions is slow, leading to a low sensor response. As the temperature is increased, O^- ions form more rapidly and react with CO at an enhanced rate. However, the rate of O^- formation cannot rise indefinitely, as it is limited by the concentration of unoccupied surface sites. Moreover, the reverse reaction, shown in Eq. (2), also increases with temperature, resulting in K_O decreasing at sufficiently high temperature values. Although the probability of a CO molecule reacting with an O^- ion is increased at these temperatures, the lowered concentration of O^- ions leads to a suppressed reaction rate and a corresponding decrease in the sensor response.

4.5. Fitting the theoretical model to response and recovery curves

Once estimates for α and K_O have been obtained, it is possible to fit the model to response and recovery traces using Eq. (13) and Eq. (17) respectively. However, it is still necessary to manually input estimates for two of three further parameters, namely k_{-1}, k_{r1} and k_{r2}. The third of these variables can be calculated from the other two using the measured gradient from Fig. 4 in conjunction with Eq. (21). It is worth remembering that the linear trends observed in Fig. 4 are indicative of a k_{r2} value that is far greater in magnitude than $k_{r1}P_{CO}/P_{TOT}$. A further observation is that the best fits to the response and recovery curves are obtained by assuming that k_{r2} is much larger than k_{-1}. These approximations vastly simplify the process of selecting appropriate parameter values as they remove all dependence on k_{r2} from the pre-exponential factors in both Eq. (13) and Eq. (17). In effect, the k_{r2} dependence is confined to the exponent itself, and therefore only influences the response or recovery at low values of t. Consequently, fits to the response and recovery curves are only weakly affected by even large changes in k_{r2}. It is therefore only necessary to estimate a single parameter accurately, simplifying the fitting procedure and ensuring that it delivers

unique solutions. The resulting fits to the response and recovery traces at a CO concentration of 200 ppm are displayed in Fig. 7 and Fig. 8 respectively; data are normalised with respect to the starting resistance and successive curves are arbitrarily offset to aid comparison.

The plots clearly show that the response and recovery rates increase with temperature. It has been noted that Eq. (12), describing the time variation of θ_{CO}, is an approximation which is only justified when θ_O changes sufficiently slowly. It is demonstrated in the Supplementary Information that this is indeed the case for every response and recovery curve described in this investigation.

4.6. Estimation of activation energies for the surface reactions

Having fitted the theoretical model to the resistance measurements, it is possible to further investigate the physics of the surface reactions by comparing the reaction parameters obtained under different conditions. Firstly, the temperature-dependence of R_0, the resistance in the absence of surface ions, is considered. When the applied electric potential is sufficiently low, thermoelectronic emission theory dictates that for a porous semiconductor containing a concentration n_s of free surface electrons, the resistance, R, obeys the relation [28].

$$R \propto \frac{\sqrt{T}}{n_S} \tag{22}$$

It is known that in a typical semiconductor, n_S is given by [31]

$$n_S = N_C \exp\left(-\frac{E_{C,S}-E_F}{k_B T}\right) \tag{23}$$

where E_F and $E_{C,S}$ are the Fermi Energy and the energy of the conduction band minimum at the surface, respectively, and k_B is Boltzmann's constant. The pre-exponential factor, N_C, scales in direct proportion to $T^{3/2}$. The value of $E_{C,S}$ depends on the concentration of ions adsorbed at the surface, which is a temperature-dependent quantity. However, in the absence of O^- or CO_2^- ions, the magnitude of the surface potential barrier, and therefore $E_{C,S}$, is assumed to remain constant as the temperature is varied. In addition, if the range of measured temperatures is sufficiently small, the variation of E_F may also be neglected. Combining Eq. (22) with Eq. (23) and imposing the condition that no surface ions are present, one obtains the expression

$$\ln(R_0) + \ln(T) = \frac{E_{C,S} - E_F}{k_B T} + A \tag{24}$$

where A is a temperature-independent constant. If, as predicted, $E_{C,S}$-E_F remains constant over the measured range of temperatures, a plot of the sum of $\ln(R_0)$ and $\ln(T)$ as a function of $1/T$ ought to be linear with gradient equal to $(E_{C,S}-E_F)/k_B$. Fig. 9, which utilises the $\ln(R_0)$ estimates obtained from Fig. 3, demonstrates that this linearity exists within the experimental error, and the gradient yields an estimate of 590 ± 90 meV for $E_{C,S}$-E_F. It should be

emphasised that this value is only applicable in the absence of surface ions, and is increased by an amount equal to $\alpha\theta_O^2 k_B T$ when such ions are present.

The temperature dependences of rate constants may be studied in a similar manner. It is often found that the rate of a chemical reaction exhibits an exponential dependence on temperature, so useful kinetic parameters may be obtained from an Arrhenius plot, wherein the natural logarithm of the rate constant is plotted as a function of $1/T$. The rate constant, k_i, is related to the molar activation energy, E_i, of the reaction through the equation

$$\ln(k_i) = \ln\left(\lim_{T\to\infty} k_i\right) - \frac{E_i}{R_M T} \qquad (25)$$

where R_M is the molar gas constant. For instance, the energy barrier for the formation of O^- ions from molecular oxygen may be deduced by constructing an Arrhenius plot for rate constant k_1, as shown in Fig. 10. Using values obtained from the measured response at a CO concentration of 200 ppm, the activation energy is estimated as 72 ± 9 kJ mol^{-1}. If the recovery curves are considered instead, an alternative estimate of 63 ± 10 kJ mol^{-1} is obtained. These values are of similar magnitude to the activation energies of similar processes reported elsewhere; separate investigations into the ionisation of oxygen at the surface of ZnO report activation energies of 69 kJ mol^{-1} [32] and 83 kJ mol^{-1} [33], while another study calculates the energy barrier for the formation of O^- ions on TiO_2 as approximately 77 kJ mol^{-1} [34].

Fig. 11 depicts an Arrhenius plot for the rate constant k_{r1}, corresponding to the reaction of O^- ions with CO. Considering the response and recovery curves separately, as before, it is apparent that the expected linearity exists for both sets of results. Using Eq. (25) to interpret Fig. 11, the response curves yield an activation energy estimate of 54 ± 9 kJ mol^{-1}, whereas the recovery curves lead to a value of 42 ± 7 kJ mol^{-1}. These estimates are consistent with previous research, in which activation energies of 39–42 kJ mol^{-1} have been deduced through measurement and computational modelling [35–38].

Conclusions

Through consideration of the kinetics of the surface reactions, a mathematical model has been developed to describe the measured response of a zinc oxide nanosheet-based sensor to carbon monoxide gas. Fitting of the response and recovery curves was facilitated by assuming the carbon monoxide reacts with surface oxygen ions via an Eley-Rideal mechanism, neglecting the reactions of carbon monoxide adsorbed at bare surface sites.

To complement the response measurements, additional tests were conducted to explore the physics of the system in the absence of carbon monoxide. From these experiments, it became possible to calculate the surface concentration of oxygen ions at a particular electrical resistance, providing the means to determine the rate of reactions occurring at the zinc oxide surface. Furthermore, comparison between the estimates acquired at different working temperatures allowed the activation energies for these processes to be evaluated. In

particular, the activation energy for the reaction between O^- ions and carbon monoxide was estimated as 54 ± 9 kJ mol^{-1} or 42 ± 7 kJ mol^{-1} from the response and recovery curves respectively. The energy barrier for the formation of O^- ions was found to be 72 ± 9 kJ mol^{-1} from the sensor response and 63 ± 10 kJ mol^{-1} from the recovery. These values are comparable to estimates existing in the literature, corroborating the validity of both the model and the experimental procedure. In the absence of surface ions, the energy difference between the Fermi level and the conduction band minimum at the surface is estimated as 590 ± 90 meV.

Acknowledgements

The Authors are grateful for the support provided by the Knowledge Economy and Skills Scholarships project, Haydale Ltd and the University Research Fellowship scheme of the Royal Society.

References

[1] Q. Yu, K. Wang, C. Luan, Y. Geng, G. Lian, D. Cui, *A dual-functional highly responsive gas sensor fabricated from SnO2 porous nanosolid,* Sens. Actuators B 159 (2011) 271– 276.

[2] J. Gong, Q. Chen, W. Fei, S. Seal, *Micromachined nanocrystalline SnO2 chemical gas sensors for electronic nose,* Sens. Actuators B 102 (2004) 117–125.

[3] J. Lee, D. H. Kim, S-H. Hong, J.Y. Jho, *A hydrogen gas sensor employing vertically aligned TiO2 nanotube arrays prepared by template-assisted method,* Sens. Actuators B 160 (2011) 1494– 1498.

[4] S. Wang, Z-X. Lin, W-H. Wang, C.L. Kuo, K.C. Hwang, C-C. Hong, *Self-regenerating photocatalytic sensor based on dielectrophoretically assembled TiO2 nanowires for chemical vapor sensing,* Sens. Actuators B 194 (2014) 1– 9.

[5] J.J. Hassan, M.A. Mahdi, C.W. Chin, H. Abu-Hassan, Z. Hassan, *A high-sensitivity room-temperature hydrogen gas sensor based on oblique and vertical ZnO nanorod arrays,* Sens. Actuators B 176 (2013) 360– 367.

[6] S.K. Lim, S-H. Hwang, S. Kim, H. Park, *Preparation of ZnO nanorods by microemulsion synthesis and their application as a CO gas sensor,* Sensors and Actuators B 160 (2011) 94–98.

[7] B.P.J de Lacy Costello, R.J. Ewen, N. Guernion, N.M. Ratcliffe, *Highly sensitive mixed oxide sensors for the detection of ethanol*, Sens. Actuators B 87 (2002) 207–210.

[8] Y. Hu, H. Lee, S. Kim, M. Yun, *A highly selective chemical sensor array based on nanowire/nanostructure for gas identification,* Sens. Actuators B 181 (2013) 424–431.

[9] L. Chambon, J.P. Germain, A. Pauly, V. Demarne, A. Grisel, *A metallic oxide gas sensor array for a selective detection of the CO and NH3 gases,* Sens. Actuators B 60 (1999) 138–147.

[10] J. Courbat, D. Briand, L. Yue, S. Raible, N.F. de Rooij, *Drop-coated metal-oxide gas sensor on polyimide foil with reduced power consumption for wireless application,* Sens. Actuators B 161 (2012) 862–868.

[11] S.E. Moon, H-K. Lee, N-J. Choi, J. Lee, C.A. Choi, W.S. Yang, J. Kim, J.J. Jong, D-J. Yoo, *Low power consumption micro C2H5OH gas sensor based on micro-heater and screen printing technique,* Sens. Actuators B 187 (2013) 598–603.

[12] T. Stoycheva, S. Vallejos, C. Blackman, S.J.A. Moniz, J. Calderer, X. Correig, *Important considerations for effective gas sensors based on metal oxide nanoneedles film,* Sens. Actuators B 161 (2012) 406–413.

[13] S. Mubeen, M. Moskovits, *Gate-Tunable Surface Processes on a Single-Nanowire Field-Effect Transistor,* Adv. Mater. 23 (2011) 2306–2312.

[14] Z. Fan, J.G. Lu, *Gate-refreshable nanowire chemical sensors,* Appl. Phys. Lett. 86 (2005)123510.

[15] A. Setkus, *Heterogeneous reaction rate based description of the response kinetics in metal oxide gas sensors,* Sens. Actuators B 87 (2002) 346–357.

[16] K. Grass, H.-G. Lintz, *The Kinetics of Carbon Monoxide Oxidation on Tin(IV) Oxide Supported Platinum Catalysts*, J. Catal. 172 (1997) 446–452.

[17] V.P. Zhdanov, *Impact of surface science on the understanding of kinetics of heterogeneous catalytic reactions*, Surf. Sci. 500 (2002) 966–985.

[18] S. Bai, T. Guo, D. Li, R. Luo, A. Chen, C.C. Liu, *Intrinsic sensing properties of the flower-like ZnO nanostructures,* Sens. Actuators B 182 (2013) 747–754.

[19] S. Nakata, S. Akakabe, M. Nakasuji, K. Yoshikawa, *Gas Sensing Based on a Nonlinear Response: Discrimination between Hydrocarbons and Quantification of Individual Components in a Gas Mixture*, Anal. Chem. 68 (1996) 2067–2072.

[20] H. Busse, M.R. Voss, D. Jerdev, B.E. Koel, M.T. Paffet, *Adsorption and reaction of gaseous H(D) atoms with D(H) adatoms on Pt(1 1 1) and Sn/Pt(1 1 1) surface alloys*, Surf. Sci. 490 (2001) 133–144.

[21] I. Kocemba, J. Rynkowski, *The influence of catalytic activity on the response of Pt/SnO2 gas sensors to carbon monoxide and hydrogen,* Sens. Actuators B 155 (2011) 659–666.

[22] K. Darcovich, F.F. Garcia, C.A. Jeffrey, J.J. Tunney, M.L. Post, *Coupled microstructural and transport effects in n-type sensor response modeling for thin layers,* Sens. Actuators A 147 (2008) 378–386.

[23] A. Fort, M. Mugnaini, S. Rocchi, M.B. Serrano-Santos, V. Vignoli, R. Spinicci, *Simplified models for SnO2 sensors during chemical and thermal transients in mixtures of inert, oxidizing and reducing gases,* Sens. Actuators B 124 (2007) 245–259.

[24] R. Ionescu, E. Llobet, S. Al-Khalifa, J.W. Gardner, X. Vilanova, J. Brezmes, X. Correig, *Response model for thermally modulated tin oxide-based microhotplate gas sensors,* Sens. Actuators B 95 (2003) 203–211.

[25] A. Varpula, S. Novikov, A. Haarahiltunen, P. Kuivalainen, *Transient characterization techniques for resistive metal-oxide gas sensors,* Sens. Actuators B 159 (2011) 12–26.

[26] S. Nakata, K. Takemura, K. Neya, *Non-linear dynamic responses of a semiconductor gas sensor: Evaluation of kinetic parameters and competition effect on the sensor response*, Sens. Actuators B 76 (2001) 436–441.

[27] F. Greuter, G. Blatter, *Electrical properties of grain boundaries in polycrystalline compound semiconductors,* Semicond. Sci. Technol. 5 (1990) 111–137.

[28] N. Barsan, U. Weimar, *Conduction Model of Metal Oxide Gas Sensors,* J. Electroceramics 7 (2001) 143–167.

[29] C. Malagù, V. Guidi, M. Stefancich, M.C. Carotta, G. Martinelli, *Model for Schottky barrier and surface states in nanostructured n-type semiconductors*, J. Appl. Phys. 91 (2002) 808–814.

[30] A. Tarat, C.J. Nettle, D.T.J. Bryant, D.R. Jones, M.W. Penny, R.A. Brown, R. Majitha, K.E. Meissner, T.G.G. Maffeis, *Microwave-assisted synthesis of layered basic zinc acetate nanosheets and their thermal decomposition into nanocrystalline ZnO,* Nanoscale Res. Lett. 9 (2014) 11–18.

[31] R. Stratton, *Surface Barriers at Semiconductor Contacts,* Proc. Phys. Soc. B 69 (1956) 513–527.

[32] J. Lagowski, E.S. Sproles Jr., H.C. Gatos, *Quantitative study of the charge transfer in chemisorption; oxygen chemisorption on ZnO,* J. Appl. Phys. 48 (1977) 3566.

[33] P.V. Bakharev, V.V. Dobrokhotov, D.N. McIlroy, *A Method for Integrating ZnO Coated Nanosprings into a Low Cost Redox-Based Chemical Sensor and Catalytic Tool for Determining Gas Phase Reaction Kinetics*, Chemosensors 2 (2014) 56–68.

[34] S. Wendt, P.T. Sprunger, E. Lira, G.K.H. Madsen, Z. Li, J.Ø. Hansen, J. Matthiesen, A. Blekinge-Rasmussen, E. Lægsgaard, B. Hammer, F. Besenbacher, *The Role of Interstitial Sites in the Ti3d Defect State in the Band Gap of Titania,* Science 320 (2008) 1755–1759.

[35] B.S. Kang, S. Kim, F. Ren, K. Ip, Y.W. Heo, B.P. Gila, C.R. Abernathy, D.P. Norton, S.J. Pearton, *Detection of CO using bulk ZnO Schottky rectifiers,* Appl. Phys. A 80 (2005) 259–261.

[36] N. Li, Q-Y. Chan, L-F. Luo, W-X. Huang, M-F. Luo, G-S. Hu, J-Q. Lu, *Kinetic study and the effect of particle size on low temperature CO oxidation over Pt/TiO2 catalysts,* Appl. Catal. B: Environ. 142– 143 (2013) 523–532.

[37] J-M. Ducéré, A. Hemeryck, A. Estève, M.D. Rouhani, G. Landa, P. Ménini, C. Tropis, A. Maisonnat, P. Fau, B. Chaudret, *A Computational Chemist Approach to Gas Sensors: Modeling the Response of SnO_2 to CO, O_2, and H_2O Gases*, J. Comput. Chem. 33 (2011) 247–258.

[38] S. Li, Z. Lu, Z. Yang, X. Chu, *The sensing mechanism of Pt-doped SnO2 surface toward CO: A first-principle study,* Sens. Actuators B 202 (2014) 83–92.

Author biographies

Daniel Raymond Jones graduated with an MSci in Physics from the University of Cambridge in 2011, and is currently working towards a PhD in Nanotechnology at Swansea University. His research focuses on the surface physics of ZnO nanostructures and their use in gas sensing applications.

Thierry Gabriel Georges Maffeïs obtained his PhD in Physics from Sheffield Hallam University in 2001, and is now an associate professor in the College of Engineering at Swansea University. His research interests include the physics of semiconductor surfaces, primarily using XPS and scanning probe microscopy.

Fig. 1. *SEM images of the zinc oxide nanosheets on the surface of the gas sensor. The platinum electrode of the sensor is visible in the top right corner of (a) and the arrangement of nanoparticles within one nanosheet is depicted in (b).*

Fig. 2. *A flowchart illustrating an iterative procedure for precisely estimating α, R_0 and K_O.*

Fig. 3. *A plot of ln(R(CO off)) as a function of θ_O(CO off)^2 at different working temperatures. The value of P_{O2}/P_{TOT} is varied between 0.05 and 0.2 in each case, in steps of 0.025.*

Fig. 4. *A plot of $1/\theta_O$(CO on) as a function of P_{CO} at different working temperature. The CO concentration is varied in the range 50–200 ppm in steps of 25 ppm.*

Fig. 5. *A plot of the magnitude of the percentage difference between the initial value of K_O used in an iteration step, K_O(in), and the K_O estimate obtained from the y-intercept of Fig. 4, K_O(out), as a function of K_O(in).*

Fig. 6. *A plot of K_O (left-hand axis) and response to 200 ppm CO (right-hand axis) as a function of temperature.*

Fig. 7. *Response curves at different working temperatures and a CO concentration of 200 ppm, fitted using Eq. (13) and altering k_{-1} and k_{r2} manually. The curves are normalised with respect to the starting resistance, and the fit to each response curve is depicted by a thick black line. Successive curves are arbitrarily offset to aid comparison.*

Fig. 8. *Recovery curves at different working temperatures and a CO concentration of 200 ppm, fitted using Eq. (17) and altering k_{-1} and k_{r2} manually. The curves are normalised with respect to the starting resistance, and the fit to each response curve is depicted by a thick black line. Successive curves are arbitrarily offset to aid comparison.*

Fig. 9. *A plot of ln(R_0)+ln(T) as a function of 1/T, constructed using estimates obtained from Fig. 3.*

Fig. 10. *A plot of ln(k_1) as a function of 1/T, constructed using response and recovery curves at a CO concentration of 200 ppm.*

Fig. 11. *A plot of ln(k_{r1}) as a function of 1/T, constructed using response and recovery curves at a CO concentration of 200 ppm.*

Highlights

- A mathematical model is developed to describe the response of a CO sensor based on ZnO nanosheets.

- A systematic series of experiments allows estimation of various reaction rate constants used in the theory.

- The experiments explore the effects of changing O_2 or CO concentration on the resistance of the sensor.

- By repeating the experiments at different temperatures, the activation energies of surface reactions are investigated.

- Arrhenius plots are used to deduce the activation energy for formation of O^- ions and the reaction of these ions with CO gas.

Figure(s)

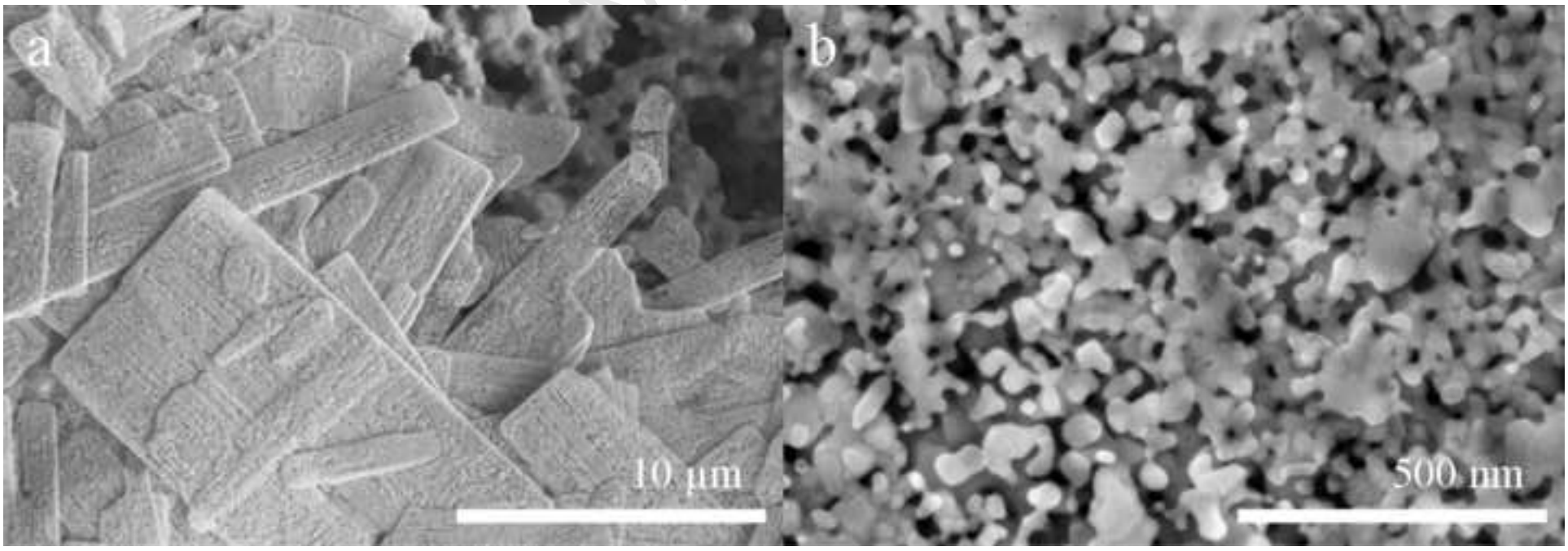

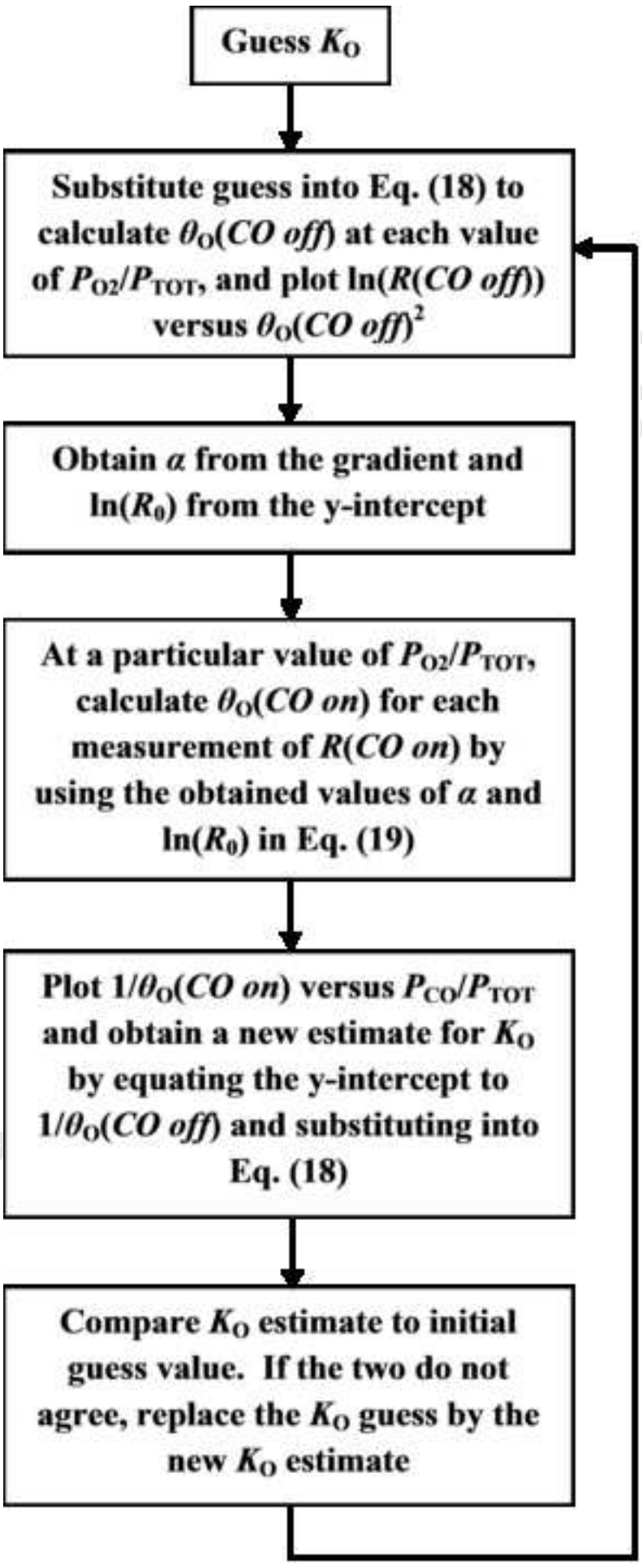

Figure(s)

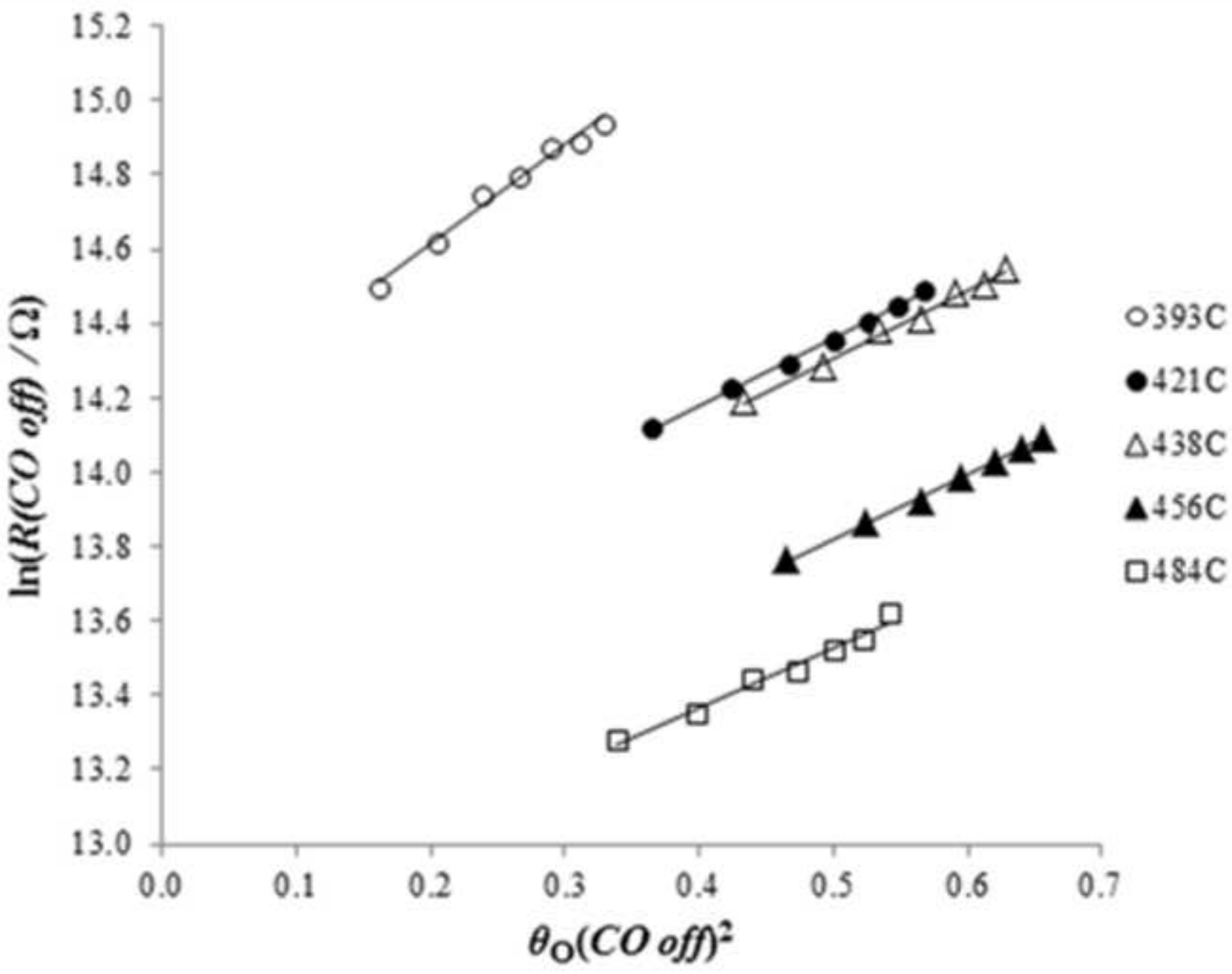
15.2
15.0
14.8
14.6
14.4
14.2
14.0
13.8
13.6
13.4
13.2
13.0
ln(R(CO off) /Ω)
0.0
0.1
0.2
0.3
0.4
0.5
0.6
0.7
θO(CO off)²
393C
421C
438C
456C
484C

Figure(s)

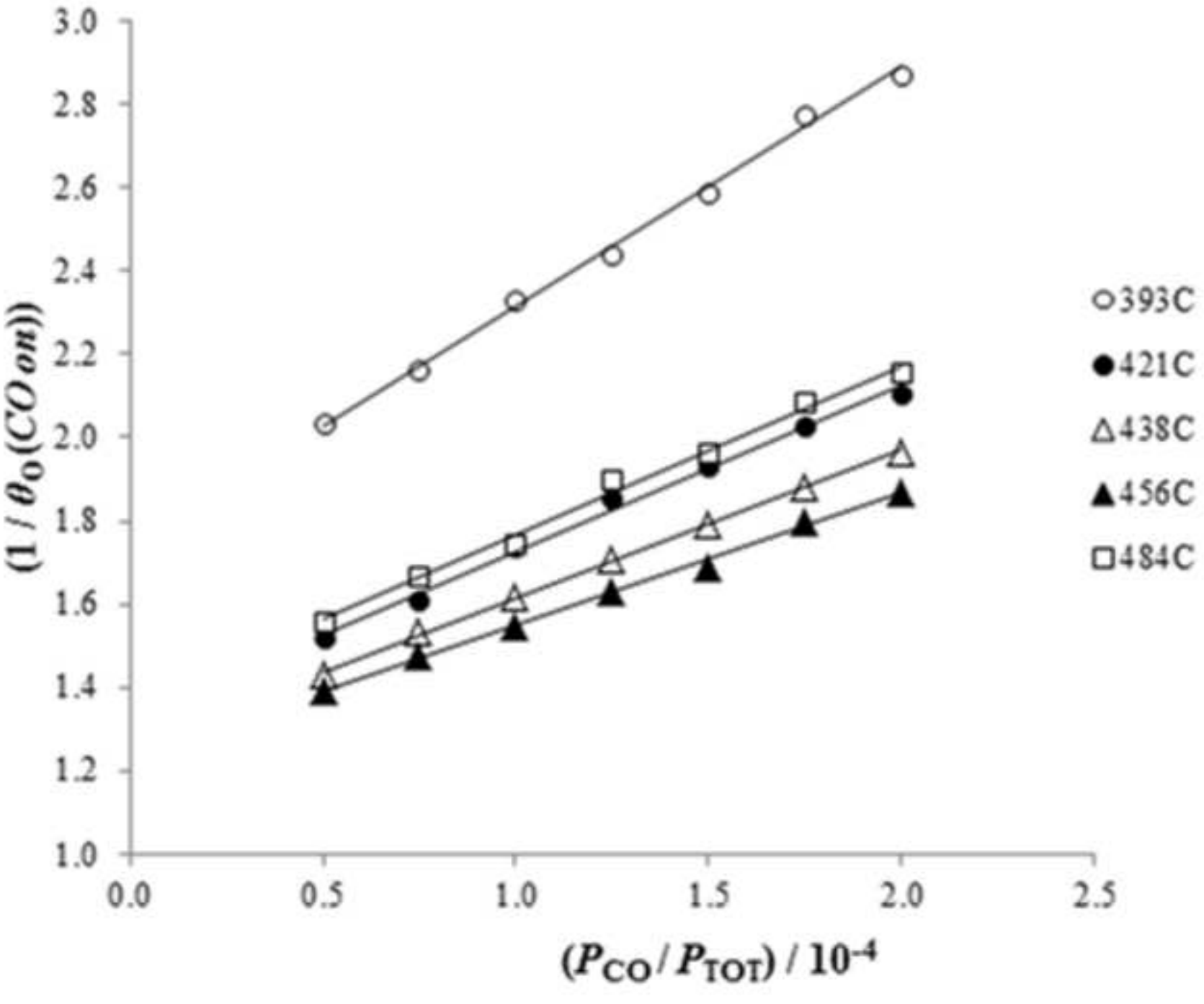
3.0
2.8
2.6
2.4
2.2
2.0
1.8
1.6
1.4
1.2
1.0
$(1 / \theta_O(CO\ on))$
0.0
0.5
1.0
1.5
2.0
2.5
$(P_{CO} / P_{TOT}) / 10^{-4}$
393C
421C
438C
456C
484C

Figure(s)

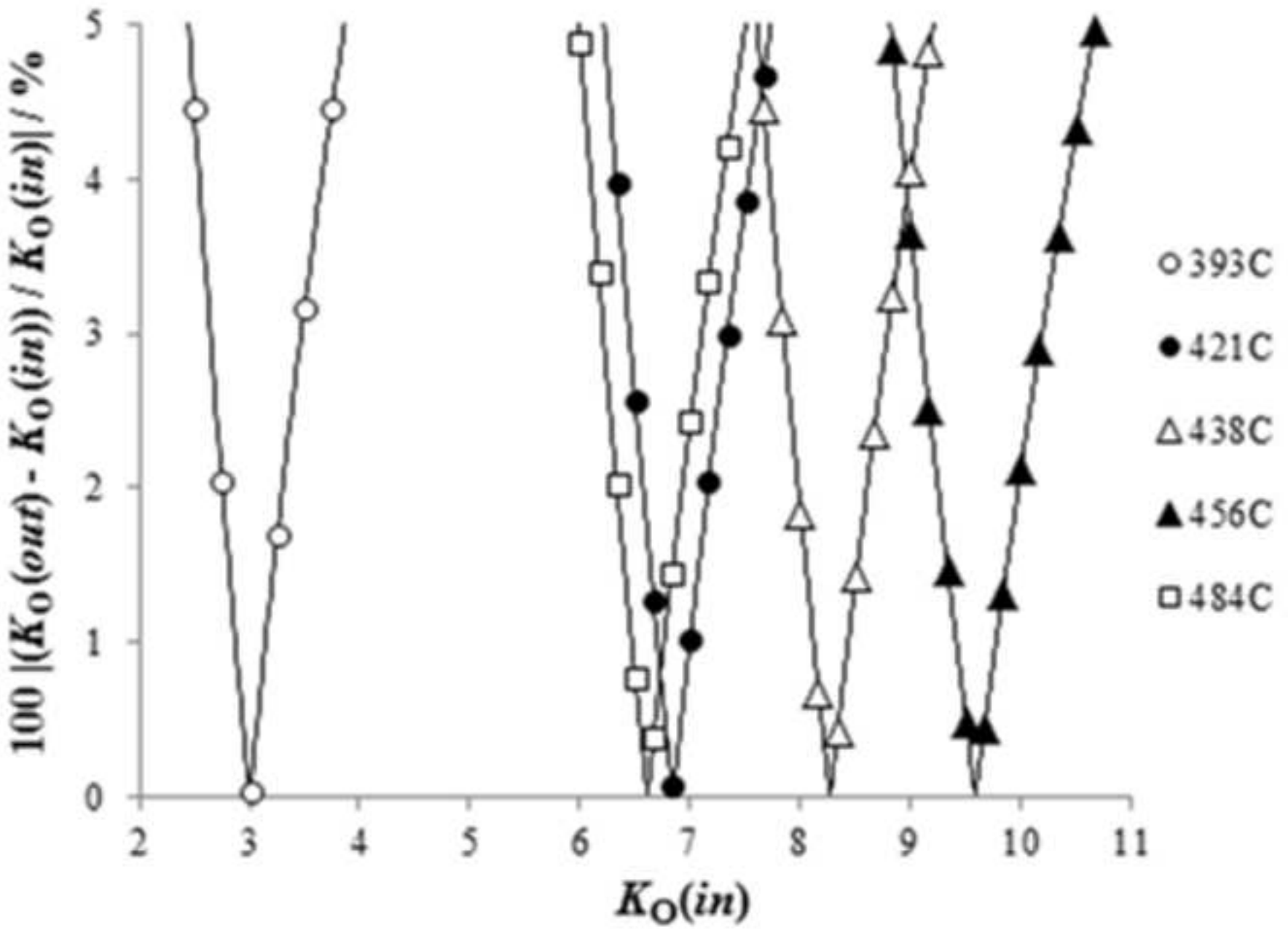
100 |(K_O(out) - K_O(in))| / K_O(in)| / %
0
1
2
3
4
5
2
3
4
5
6
7
8
9
10
11
K_O(in)
393C
421C
438C
456C
484C

Figure(s)

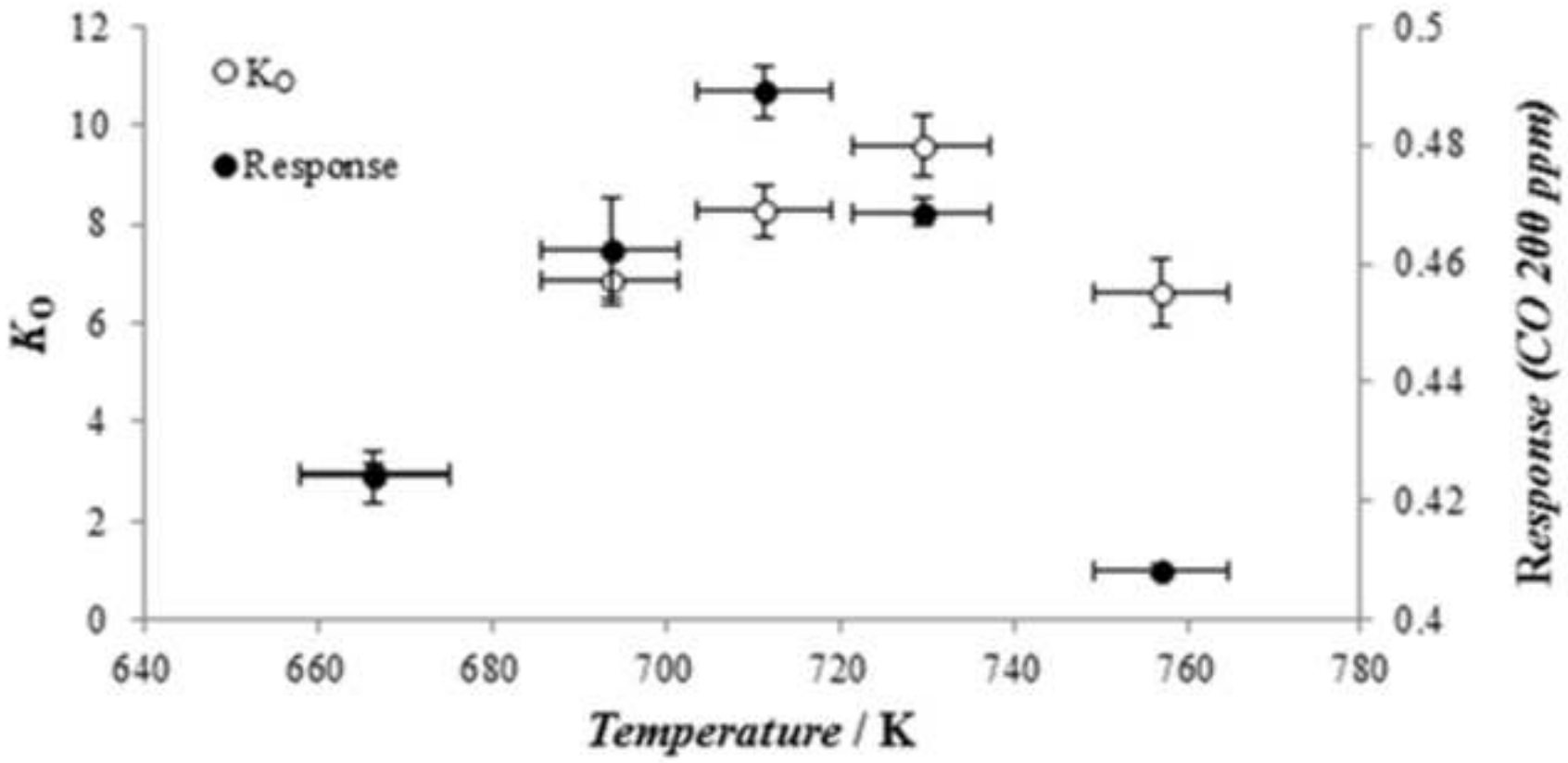
K0
Response
K0
Response (CO 200 ppm)
Temperature / K
0
2
4
6
8
10
12
0.4
0.42
0.44
0.46
0.48
0.5
640
660
680
700
720
740
760
780

Figure(s)

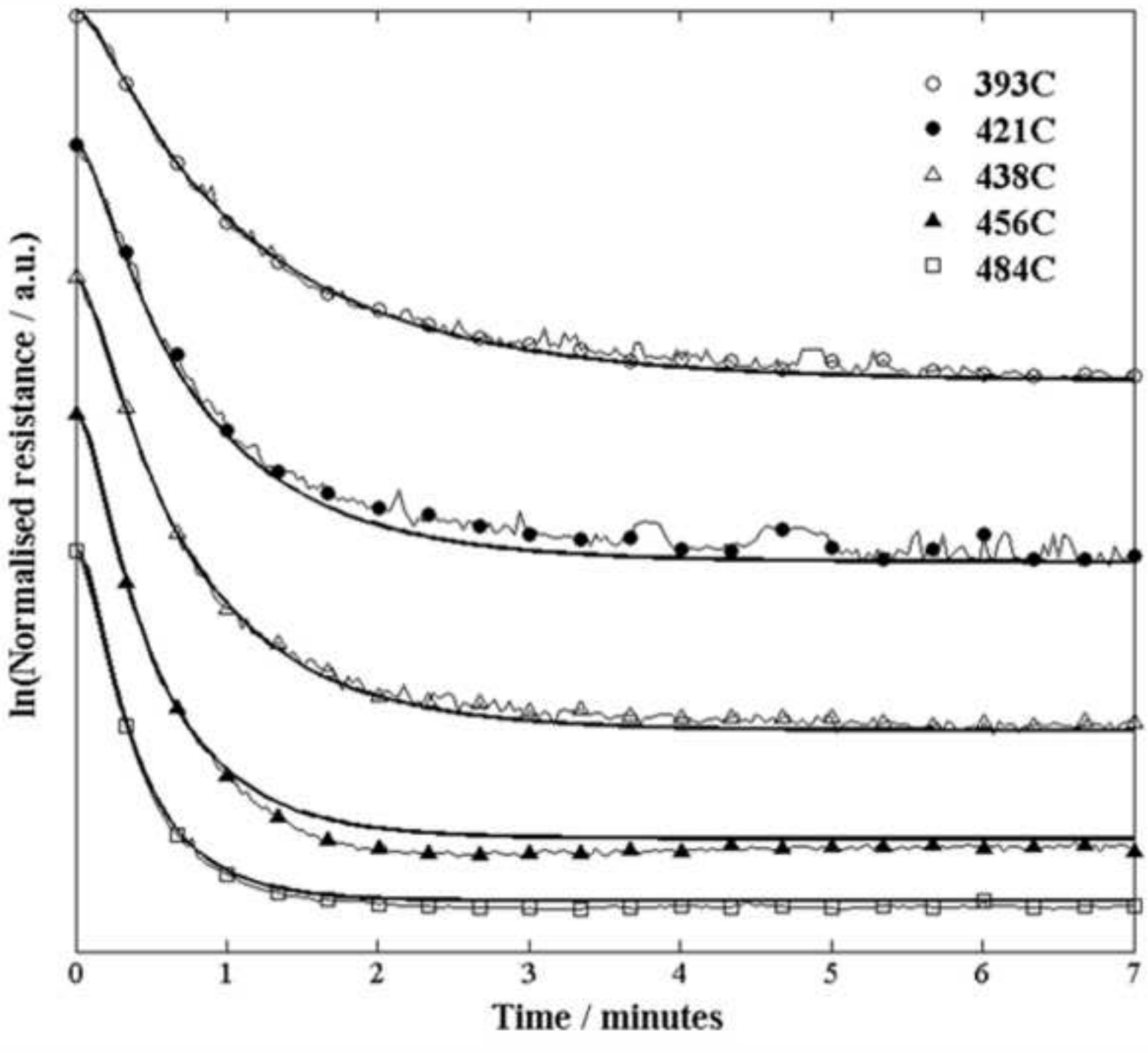
393C
421C
438C
456C
484C
ln(Normalised resistance / a.u.)
0
1
2
3
4
5
6
7
Time / minutes

Figure(s)

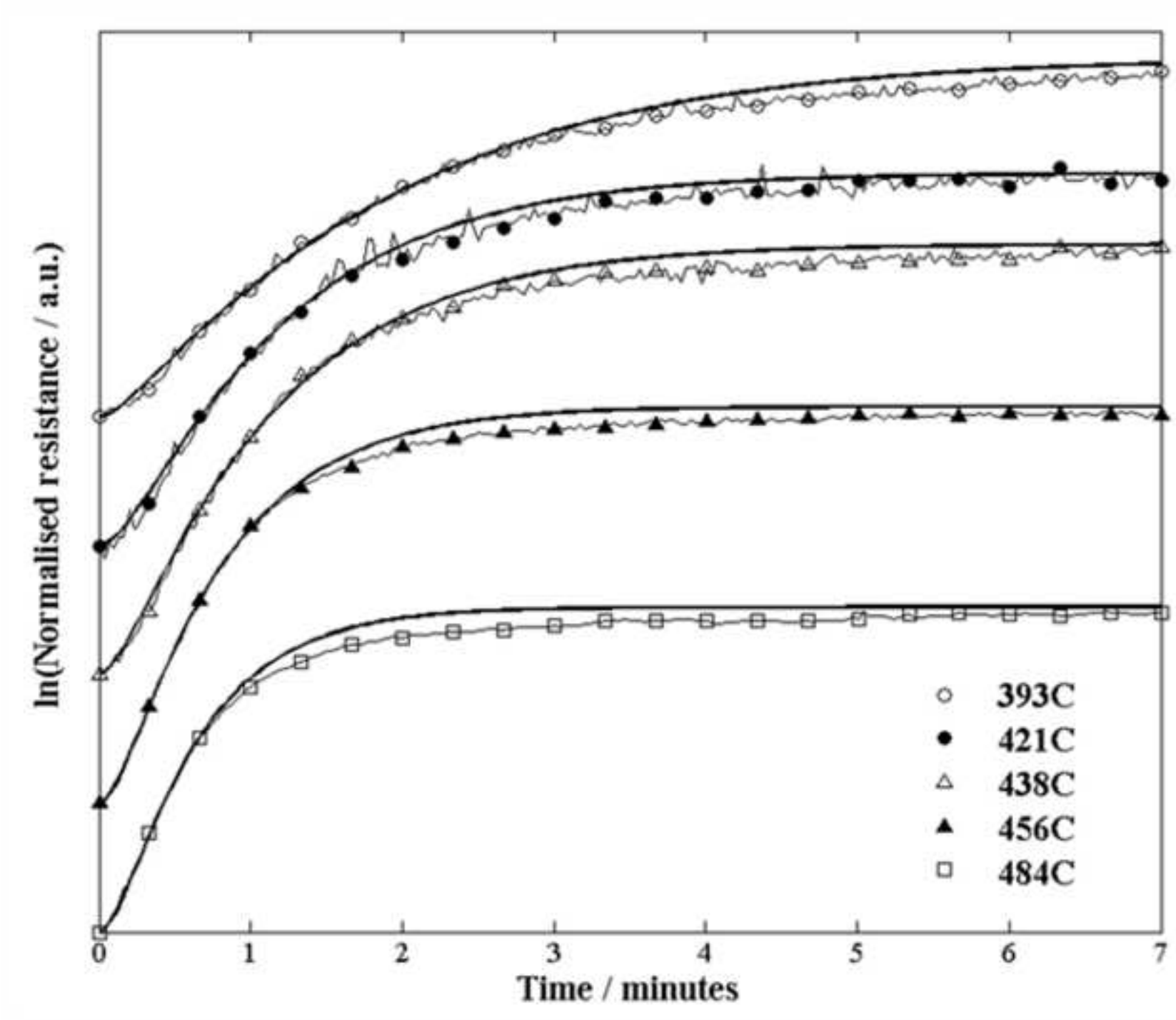
ln(Normalised resistance / a.u.)
Time / minutes
0
1
2
3
4
5
6
7
393C
421C
438C
456C
484C

Figure(s)

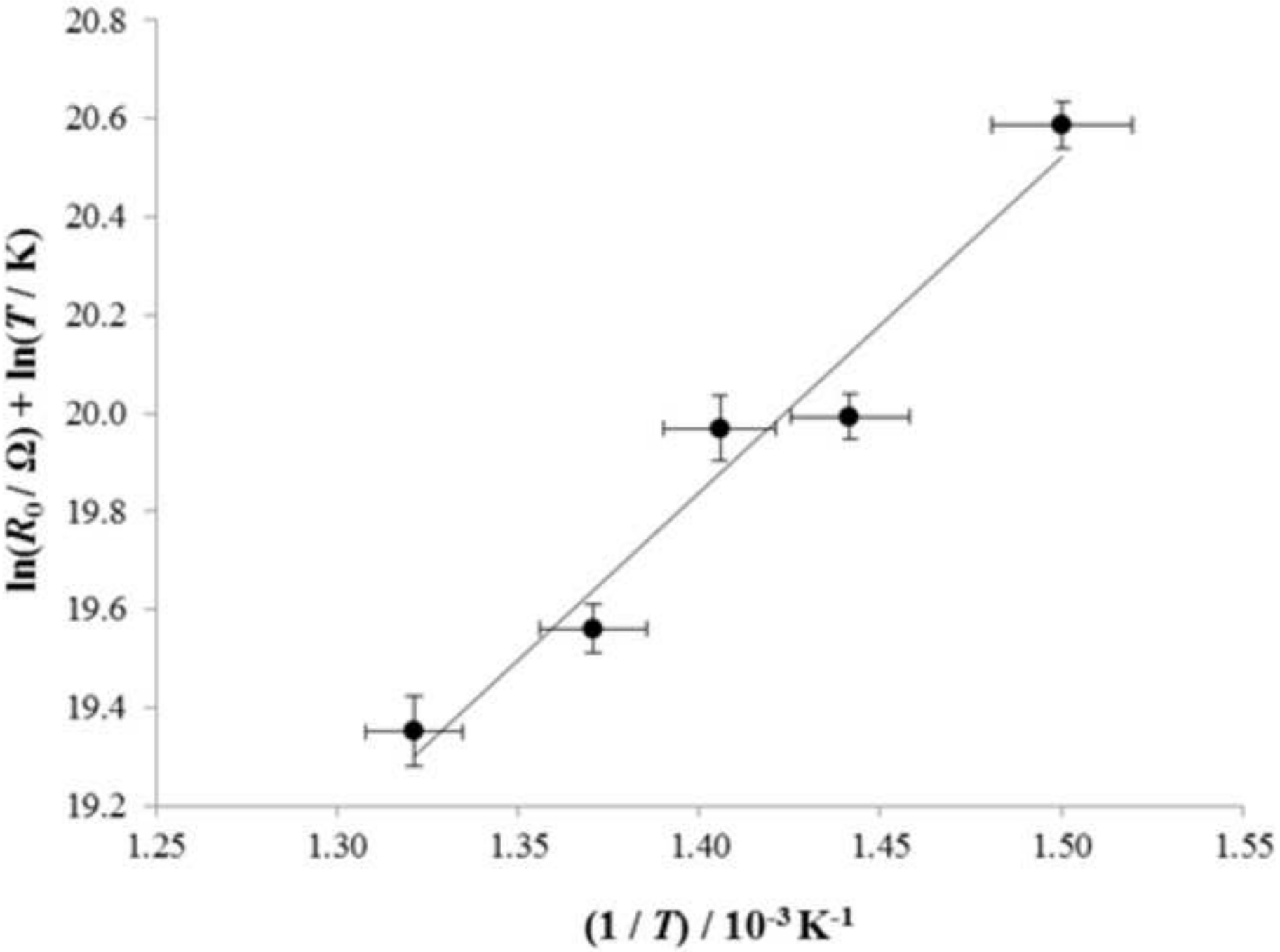
20.8
20.6
20.4
20.2
20.0
19.8
19.6
19.4
19.2
ln(R0 / Ω) + ln(T / K)
1.25
1.30
1.35
1.40
1.45
1.50
1.55
(1 / T) / 10-3 K-1

Figure(s)

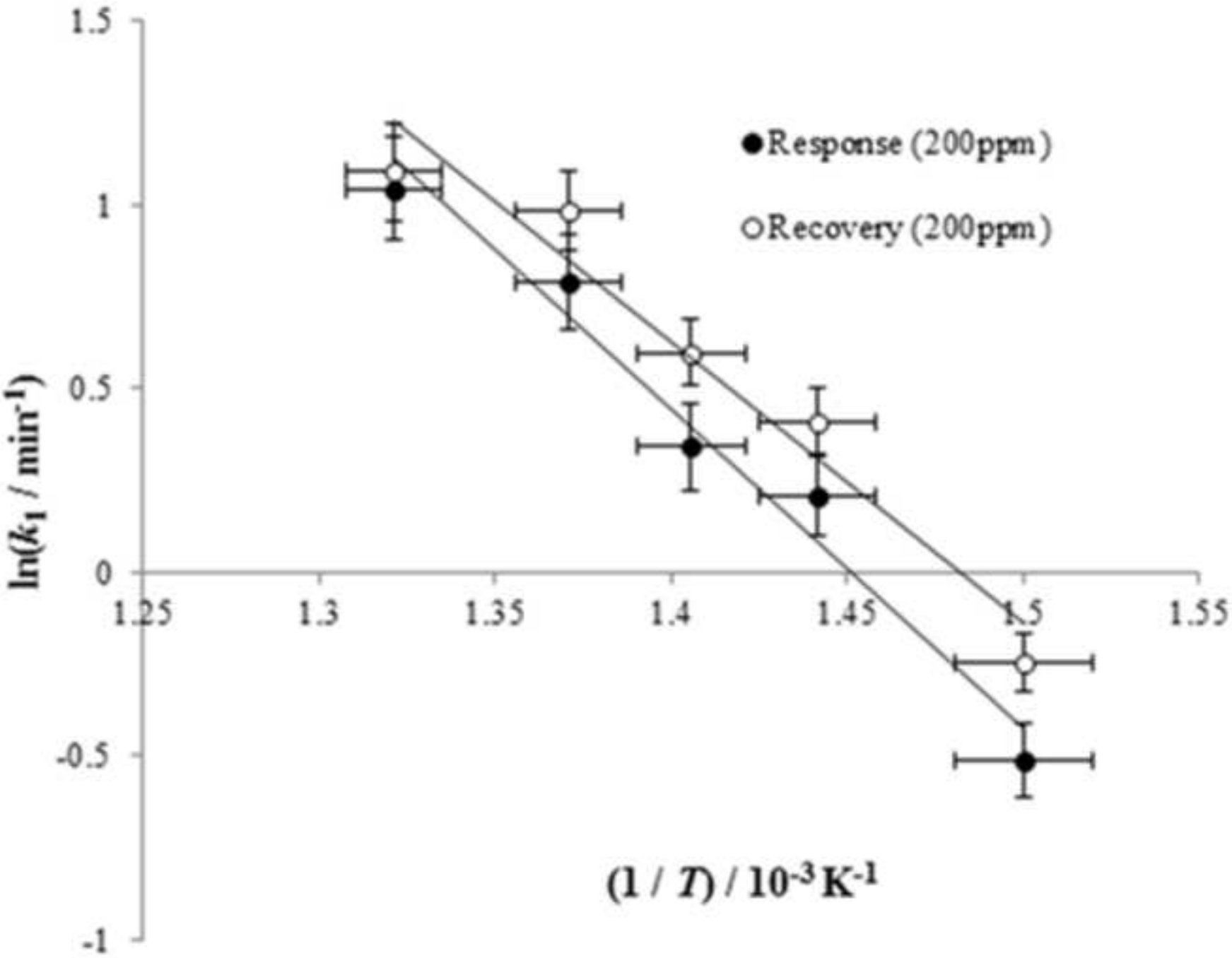
1.5
1
0.5
0
-0.5
-1
1.25
1.3
1.35
1.4
1.45
1.5
1.55
ln(k1 / min-1)
(1 / T) / 10-3 K-1
●Response (200ppm)
○Recovery (200ppm)

Figure(s)

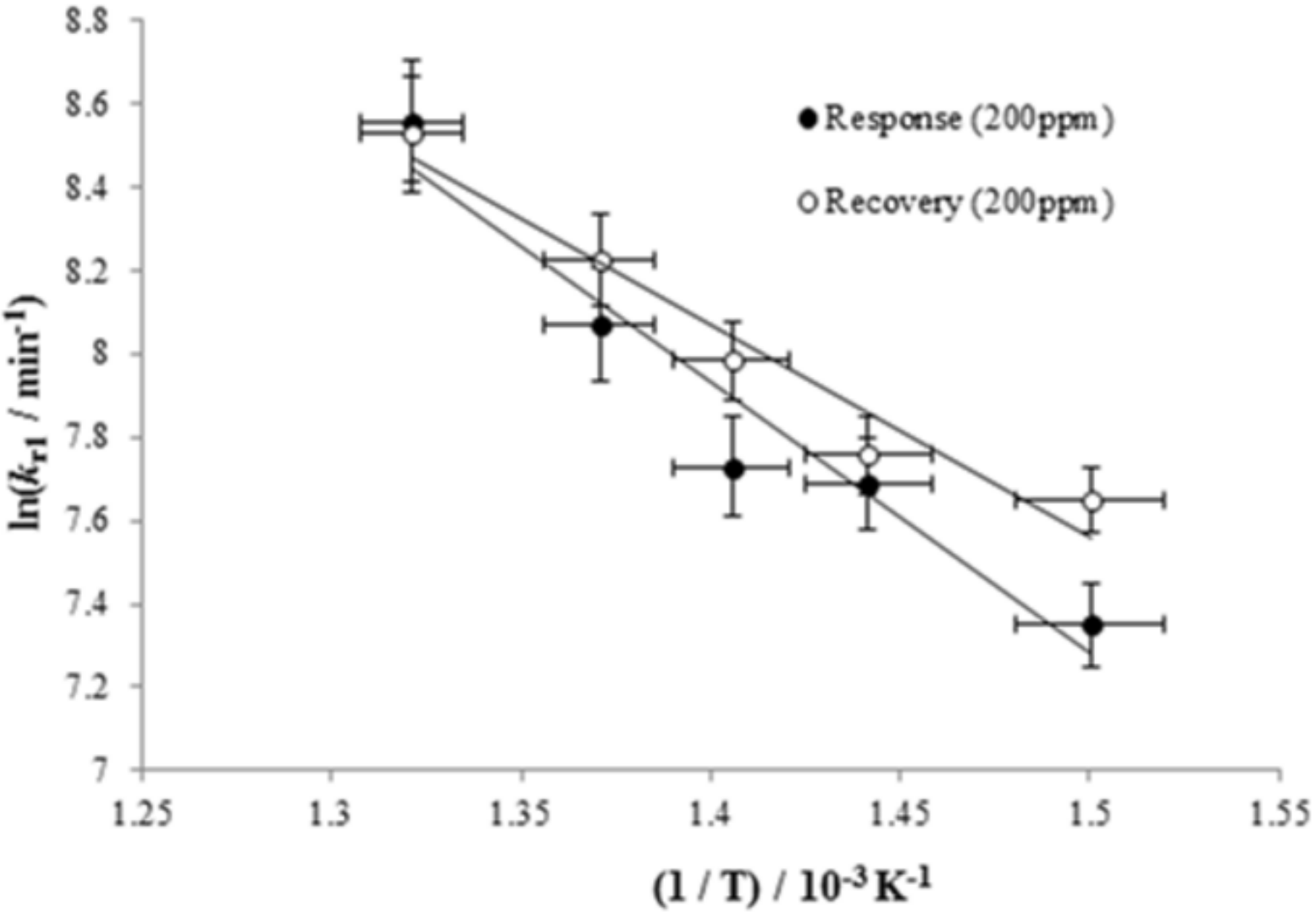
8.8
8.6
8.4
8.2
8
7.8
7.6
7.4
7.2
7
1.25
1.3
1.35
1.4
1.45
1.5
1.55
ln(k_r1 / min^-1)
(1 / T) / 10^-3 K^-1
Response (200ppm)
Recovery (200ppm)